J. Korean Soc. Ind. Appl. Math. Vol.28, No.3, 96–107, 2024 https://doi.org/10.12941/jksiam.2024.28.096

APPLICATION OF THE BIFOCUSING METHOD IN MICROWAVE IMAGING BY CONVERTING UNKNOWN MEASUREMENT DATA INTO THE CONSTANT

SANGWOO KANG[1], MINYEOB LEE[2], WON-KWANG PARK[2,†], AND SEONG-HO SON[3,4,†]

[1]GRADUATE SCHOOL OF DATA SCIENCE, PUSAN NATIONAL UNIVERSITY, BUSAN, 46241, KOREA
Email address: sangwoo.kang@pusan.ac.kr

[2]DEPARTMENT OF MATHEMATICS, KOOKMIN UNIVERSITY, SEOUL, 02707, KOREA
Email address: {lmmmy0319,†parkwk}@kookmin.ac.kr

[3]DEPARTMENT OF ICT CONVERGENCE, SOONCHUNHYANG UNIVERSITY, ASAN 31538, KOREA

[4]DEPARTMENT OF MECHANICAL ENGINEERING, SOONCHUNHYANG UNIVERSITY, ASAN, 31538, KOREA
Email address: †son@sch.ac.kr

ABSTRACT. We consider the bifocusing method (BFM) for a fast identification of small objects in microwave imaging. In many researches, it was very hard to measure the scattering parameter data if the location of the transmitter and the receiver is the same. Due to this reason, the imaging function of BFM has mainly been designed by converting unknown measurement data into the zero constant; this approach has yielded reliable imaging results, but the theoretical reason for this conversion has not been investigated yet. In this study, we converted unknown measurement data to a fixed constant and applied the BFM to retrieve small objects. To demonstrate the effect of the converted constant, we show that the imaging function of the BFM can be represented in terms of an infinite series of the Bessel functions of an integer order, antenna setting, material properties, and applied constant. Based on the theoretical result, we concluded that converting unknown measurement data to constant zero guarantees good imaging results, including the unique determination of the objects. Simulation results obtained with synthetic and real data support the theoretical result.

1. INTRODUCTION

The detection and visualization of unknown objects completely embedded in a homogeneous region or material is an interesting research subject in inverse scattering problems and microwave imaging. In this context, various reconstruction algorithms have been developed, and these algorithms are generally classified as quantitative (or iterative) and qualitative (or non-iterative) methods. Recently, various remarkable algorithms have been developed and applied to various problems. For example, Newton-type algorithm for shape reconstruction of

Received July 30 2024; Accepted September 24 2024; Published online September 25 2024.
2000 *Mathematics Subject Classification.* 78A46.
Key words and phrases. Bifocusing Method, Scattering Parameter, Microwave Imaging, Simulation Results.
† Corresponding authors.

arc-like perfectly conducting crack [1], Gauss-Newton method in electrical impedance tomography [2], distorted Born [3] iterative method for reconstructing parameter distribution, Nelder-Mead simplex method for identifying a perfect conductor in a two-layered medium [4], level set method for shape reconstruction of arbitrary shaped targets [5], direct and orthogonality sampling methods for object detection [6, 7], factorization method for breast cancer detection [8], Kirchhoff and subspace migration algorithms in microwave imaging [9, 10], MUltiple Signal Classification for anomaly detection [11], linear sampling method for identifying unknown scatterers from Fresnel and Manitoba databases [12], and topological derivative for a fast identification of small conductivity inclusion [13].

Among the remarkable techniques, the bifocusing method (BFM), which is categorized as a qualitative technique, has been gaining attention for its potential to effectively address the inverse scattering problem in microwave imaging. It has been applied to various problems in tomographic imaging [14], ultra-wide-band tomographic radar imaging [15], damage detection of concrete void [16], and localization of small scatterers [17]. Prior research has confirmed that the BFM is a fast and effective method for identifying unknown objects and is stable against random noise. For a proper application of the BFM in microwave imaging with multi-static measurement configurations, complete elements of the scattering matrix must be known. However, in many applications, the diagonal elements of the matrix cannot be measured when the transmitting and receiving antennas are installed at the same location, as explained in [18]. Let us emphasize that without a priori information of the objects, unknown measurement data cannot be estimated. Due to this reason, unknown measurement data was typically converted to a constant zero, as done by [19, 20, 21, 22, 23, 24]. Notice that if one converts the unknown measurement data into a nonzero constant, the obtained result is poor when the absolute value of the constant is not small enough because the imaging performance of the BFM depends significantly on the constant. However, to the best of our knowledge, the effect of the converted constant has not been investigated satisfactorily from the perspective of its mathematical theory.

In this study, we consider the application of the BFM for a fast imaging of small objects in microwave imaging. Unlike the previous studies, we converted the unknown diagonal elements of the scattering matrix into a fixed constant and introduced an imaging function of the BFM. To show the influence of the converted constant, we established the mathematical theory by showing that the imaging function can be represented by an infinite series of the Bessel function of integer order, the antenna settings, the material properties, and the converted constant. Based on the theoretical result, we demonstrated that the imaging performance depends significantly on the converted constant and that the selection of zero constant guarantees good imaging results, including unique determination of objects. The theoretical result was verified through the numerical simulation results obtained with synthetic and real data.

The remaining part of this study is organized as follows. In Section 2, we introduce the problem setting, the basic concept of the scattered field $S-$ parameter in the presence of small objects, and the imaging function of the BFM by converting unknown diagonal elements of the scattering matrix as a fixed constant. Section 3 explores the mathematical structure of the imaging function by establishing the relationship with an infinite series of the Bessel functions,

the antenna settings, the material properties, and the converted constant. Based on the theoretical result, we conclude that conversion to zero constant is the best choice to identify the objects, and this conversion guarantees unique determination. Section 4 reports the simulation results obtained with synthetic and real data to support the theoretical result. Section 5 presents a short conclusion and suggests directions for future studies.

2. Scattering Matrix and Imaging Function for the Bifocusing Method

2.1. **Problem Setting and Scattering Matrix.** Assume that there exists a set of well-separated small objects D_s, $s = 1, 2, \ldots, S$, in a two-dimensional (2D) homogeneous region Ω. We denote D as the collection of D_s and assume that D and Ω are nonmagnetic. Correspondingly, we set the value of magnetic permeability as $\mu(\mathbf{r}) = \mu_0 = 4\pi \times 10^{-7}\,\mathrm{H/m}$ for every $\mathbf{r} \in \Omega$. Further, we assume that every material is characterized by its dielectric permittivity and electrical conductivity at a given angular frequency $\omega = 2\pi f$. Let ε_{b} and ε_s be the values of the permittivity of Ω and D_s, respectively. Analogously, σ_{b} and σ_s denote the conductivity of Ω and D_s, respectively. Then, we define the following piecewise constants:

$$\varepsilon(\mathbf{r}) = \begin{cases} \varepsilon_s, & \mathbf{r} \in D_s \\ \varepsilon_{\mathrm{b}}, & \mathbf{r} \in \Omega \backslash \overline{D} \end{cases} \quad \text{and} \quad \sigma(\mathbf{r}) = \begin{cases} \sigma_s, & \mathbf{r} \in D_s \\ \sigma_{\mathrm{b}}, & \mathbf{r} \in \Omega \backslash \overline{D}, \end{cases}$$

and denote $k_{\mathrm{b}} = \omega\sqrt{\mu_0(\varepsilon_{\mathrm{b}} - i\sigma_{\mathrm{b}}/\omega)}$ as the background wavenumber. Throughout this study, we assumed that the following relations hold: for $s = 1, 2, \ldots, S$,

$$\varepsilon_{\mathrm{b}} \gg \frac{\sigma_{\mathrm{b}}}{\omega} \quad \text{and} \quad \left(\sqrt{\frac{\varepsilon_s}{\varepsilon_{\mathrm{b}}}} - 1\right)\mathrm{diam}(D_s) < \frac{\lambda}{2}, \tag{2.1}$$

where λ denotes the given positive wavelength, and $\mathrm{diam}(D_s)$ is the diameter of D_s.

Let $\mathcal{A}_n$, $n = 1, 2, \cdots, N$, denote the dipole antenna located at $\mathbf{a}_n$ to transmit and receive signals, and let $S_{\mathrm{scat}}(n, m)$ represent the measured scattered-field $S-$parameter data with the transmitter $\mathcal{A}_m$ and receiver $\mathcal{A}_n$. From [25], $S_{\mathrm{scat}}(n, m)$ can be represented by the following integral equation formula

$$S_{\mathrm{scat}}(n, m) = \frac{ik_0^2}{4\omega\mu_0} \int_\Omega \left(\frac{\varepsilon(\mathbf{r}') - \varepsilon_{\mathrm{b}}}{\varepsilon_{\mathrm{b}}} + i\frac{\sigma(\mathbf{r}') - \sigma_{\mathrm{b}}}{\omega\varepsilon_{\mathrm{b}}}\right) \mathrm{E}^{(z)}_{\mathrm{inc}}(\mathbf{a}_m, \mathbf{r}')\mathrm{E}^{(z)}_{\mathrm{tot}}(\mathbf{r}', \mathbf{a}_n)\mathrm{d}\mathbf{r}', \tag{2.2}$$

where $k_0 = \omega\sqrt{\varepsilon_{\mathrm{b}}\mu_0}$ denotes the lossless background wavenumber; $\mathrm{E}^{(z)}_{\mathrm{inc}}(\mathbf{a}_m, \mathbf{r}')$ is the z-component of the incident electric field $\mathbf{E}_{\mathrm{inc}}(\mathbf{a}_m, \mathbf{r})$ attributed to the point current density at $\mathcal{A}_m$ that satisfies

$$\begin{cases} \nabla \times \mathbf{E}_{\mathrm{inc}}(\mathbf{a}_m, \mathbf{r}) = i\omega\mu_{\mathrm{b}}\mathbf{H}_{\mathrm{inc}}(\mathbf{a}_m, \mathbf{r}) \\ \nabla \times \mathbf{H}_{\mathrm{inc}}(\mathbf{a}_m, \mathbf{r}) = (\sigma_{\mathrm{b}} - i\omega\varepsilon_{\mathrm{b}})\mathbf{E}_{\mathrm{inc}}(\mathbf{a}_m, \mathbf{r}), \end{cases}$$

and $\mathrm{E}^{(z)}_{\mathrm{tot}}(\mathbf{r}, \mathbf{a}_n)$ is the corresponding z-component of the total electric field $\mathbf{E}_{\mathrm{tot}}(\mathbf{r}, \mathbf{a}_n)$ in the presence of D measured by the $\mathcal{A}_n$ that satisfies

$$\begin{cases} \nabla \times \mathbf{E}_{\mathrm{tot}}(\mathbf{r}, \mathbf{a}_n) = i\omega\mu_{\mathrm{b}}\mathbf{H}_{\mathrm{tot}}(\mathbf{r}, \mathbf{a}_n) \\ \nabla \times \mathbf{H}_{\mathrm{tot}}(\mathbf{r}, \mathbf{a}_n) = (\sigma(\mathbf{r}) - i\omega\varepsilon(\mathbf{r}))\mathbf{E}_{\mathrm{tot}}(\mathbf{r}, \mathbf{a}_n) \end{cases}$$

with transmission condition on ∂D_s. Here, $\mathbf{H}_{\rm inc}$ and $\mathbf{H}_{\rm tot}$ denote the magnetic field. The time-harmonic dependence $\exp(-i\omega t)$ is assumed.

It is worth to emphasize that $\mathrm{E}^{(z)}_{\rm tot}(\mathbf{r},\mathbf{a}_n)$ cannot be determined without a priori information of D. Hence, it is very difficult to apply (2.2) directly for designing the imaging function. We emphasize that since the condition (2.1) holds, it is possible to apply the Born approximation $\mathrm{E}^{(z)}_{\rm tot}(\mathbf{r}',\mathbf{a}_n)\approx \mathrm{E}^{(z)}_{\rm inc}(\mathbf{r}',\mathbf{a}_n)$. Then, $S_{\rm scat}(n,m)$ can be represented as the shown in following formula:

$$S_{\rm scat}(n,m)\approx \frac{ik_0^2}{4\omega\mu_0}\int_D\left(\frac{\varepsilon(\mathbf{r}')-\varepsilon_{\rm b}}{\varepsilon_{\rm b}}+i\frac{\sigma(\mathbf{r}')-\sigma_{\rm b}}{\omega\varepsilon_{\rm b}}\right)\mathrm{E}^{(z)}_{\rm inc}(\mathbf{a}_m,\mathbf{r}')\mathrm{E}^{(z)}_{\rm inc}(\mathbf{r}',\mathbf{a}_n)\mathrm{d}\mathbf{r}'. \quad (2.3)$$

This formula will play a key role in the design and structure analysis of the imaging function.

2.2. **Imaging Function of the Bifocusing Method.** Here, we briefly introduce the imaging function of the BFM for identifying D_s from the scattering matrix $\mathbb{S}$. The elements of this matrix are measurement data $S_{\rm scat}(n,m)$.

$$\mathbb{S}=\begin{bmatrix} S_{\rm scat}(1,1) & S_{\rm scat}(1,2) & \cdots & S_{\rm scat}(1,N-1) & S_{\rm scat}(1,N)\\ S_{\rm scat}(2,1) & S_{\rm scat}(2,2) & \cdots & S_{\rm scat}(2,N-1) & S_{\rm scat}(2,N)\\ \vdots & \vdots & \ddots & \vdots & \vdots\\ S_{\rm scat}(N,1) & S_{\rm scat}(N,2) & \cdots & S_{\rm scat}(N,N-1) & S_{\rm scat}(N,N)\end{bmatrix} \quad (2.4)$$

Then, by applying the mean-value theorem to (2.3), it is seen that there exists $\mathbf{r}_s\in D_s$ such that

$$S_{\rm scat}(n,m)\approx \frac{ik_0^2}{4\omega\mu_0}\sum_{s=1}^{S}\left(\frac{\varepsilon_s-\varepsilon_{\rm b}}{\varepsilon_{\rm b}}+i\frac{\sigma_s-\sigma_{\rm b}}{\omega\varepsilon_{\rm b}}\right)\mathrm{area}(D_s)\mathrm{E}^{(z)}_{\rm inc}(\mathbf{a}_m,\mathbf{r}_s)\mathrm{E}^{(z)}_{\rm inc}(\mathbf{r}_s,\mathbf{a}_n)$$

and correspondingly, $\mathbb{S}$ can be decomposed as

$$\mathbb{S}\approx\sum_{s=1}^{S}\mathcal{O}(D_s)\begin{bmatrix}\mathrm{E}^{(z)}_{\rm inc}(\mathbf{a}_1,\mathbf{r}_s)\\ \mathrm{E}^{(z)}_{\rm inc}(\mathbf{a}_2,\mathbf{r}_s)\\ \vdots\\ \mathrm{E}^{(z)}_{\rm inc}(\mathbf{a}_N,\mathbf{r}_s)\end{bmatrix}\begin{bmatrix}\mathrm{E}^{(z)}_{\rm inc}(\mathbf{r}_s,\mathbf{a}_1) & \mathrm{E}^{(z)}_{\rm inc}(\mathbf{r}_s,\mathbf{a}_2) & \cdots & \mathrm{E}^{(z)}_{\rm inc}(\mathbf{r}_s,\mathbf{a}_N)\end{bmatrix}, \quad (2.5)$$

where

$$\mathcal{O}(D_s)=\frac{ik_0^2}{4\omega\mu_0}\left(\frac{\varepsilon_s-\varepsilon_{\rm b}}{\varepsilon_{\rm b}}+i\frac{\sigma_s-\sigma_{\rm b}}{\omega\varepsilon_{\rm b}}\right)\mathrm{area}(D_s).$$

Based on the decomposition (2.5), we can introduce the traditional imaging function of the BFM via the synthesis of inversion of two incident fields $\mathrm{E}^{(z)}_{\rm inc}(\mathbf{r},\mathbf{a}_m)$ and $\mathrm{E}^{(z)}_{\rm inc}(\mathbf{r},\mathbf{a}_n)$, $n=1,2,\ldots,N$. For each $\mathbf{r}\in\Omega$, by defining a test vector

$$\mathbf{G}(\mathbf{r})=\begin{bmatrix}\dfrac{1}{\mathrm{E}^{(z)}_{\rm inc}(\mathbf{a}_1,\mathbf{r})} & \dfrac{1}{\mathrm{E}^{(z)}_{\rm inc}(\mathbf{a}_2,\mathbf{r})} & \cdots & \dfrac{1}{\mathrm{E}^{(z)}_{\rm inc}(\mathbf{a}_N,\mathbf{r})}\end{bmatrix}, \quad (2.6)$$

the imaging function of the BFM is given by

$$\mathfrak{F}(\mathbf{r}) = |\mathbf{G}(\mathbf{r})\mathbb{S}\mathbf{G}(\mathbf{r})^T| = \left| \sum_{n=1}^{N} \sum_{m=1}^{M} \frac{S_{\text{scat}}(n,m)}{\mathrm{E}_{\text{inc}}^{(z)}(\mathbf{a}_m, \mathbf{r})\mathrm{E}_{\text{inc}}^{(z)}(\mathbf{r}, \mathbf{a}_n)} \right|.$$

Then, peaks of large magnitudes appear at $\mathbf{r} = \mathbf{r}_s \in D_s$ so that small objects can be recognized through the map of $\mathfrak{F}(\mathbf{r})$, refer to [15, 14, 16, 17].

Note that from the measurement system of the microwave machine reported in [18], the diagonal elements $S_{\text{scat}}(n,n)$, $n = 1, 2, \ldots, N$, of $\mathbb{S}$ cannot be measured because each of the N antennas is used for signal transmission, and the remaining $N-1$ antennas are used for signal reception. This means that we can use the following matrix instead of the $\mathbb{S}$

$$\begin{bmatrix} \text{unknown} & S_{\text{scat}}(1,2) & \cdots & S_{\text{scat}}(1,N-1) & S_{\text{scat}}(1,N) \\ S_{\text{scat}}(2,1) & \text{unknown} & \cdots & S_{\text{scat}}(2,N-1) & S_{\text{scat}}(2,N) \\ \vdots & \vdots & \ddots & \vdots & \vdots \\ S_{\text{scat}}(N,1) & S_{\text{scat}}(N,2) & \cdots & S_{\text{scat}}(N,N-1) & \text{unknown} \end{bmatrix}.$$

Without a priori information of the objects, the diagonal elements cannot be generated. Therefore, unknown measurement data were usually converted to a zero constant ([24, 20]). However, a reliable mathematical theory for this conversion has not been satisfactorily established. Motivated by this requirements, we defined the following scattering matrix by converting unknown data to a fixed constant C

$$\mathbb{K}(C) = \begin{bmatrix} C & S_{\text{scat}}(1,2) & \cdots & S_{\text{scat}}(1,N-1) & S_{\text{scat}}(1,N) \\ S_{\text{scat}}(2,1) & C & \cdots & S_{\text{scat}}(2,N-1) & S_{\text{scat}}(2,N) \\ \vdots & \vdots & \ddots & \vdots & \vdots \\ S_{\text{scat}}(N,1) & S_{\text{scat}}(N,2) & \cdots & S_{\text{scat}}(N,N-1) & C \end{bmatrix}$$

and applied the following imaging function of the BFM

$$\mathfrak{F}_{\text{BFM}}(\mathbf{r}, C) = |\mathbf{G}(\mathbf{r})\mathbb{K}(C)\mathbf{G}(\mathbf{r})^T|. \tag{2.7}$$

3. Structure of the Imaging Function and the Best Selection of Constant

Following the simulation result, we can identify D_s through the map of $\mathfrak{F}_{\text{BFM}}(\mathbf{r}, C)$ for some particular selection of C. We established the mathematical theory of the imaging function $\mathfrak{F}_{\text{BFM}}(\mathbf{r}, C)$ to explain the effect of C and to explain why the selection $C = 0$ is the best choice that guarantees the unique determination of the objects. To this end, we derived the following result. Although the derivation is similar to the recent studies [24, 20], we have included the derivation for the convenience of the readers.

Theorem 3.1 (Structure of the Imaging Function)**.** *Let* $\boldsymbol{\theta}_n = \mathbf{a}_n/|\mathbf{a}_n| = \mathbf{a}_n/R = (\cos\theta_n, \sin\theta_n)$, $\mathbf{r} = |\mathbf{r}|(\cos\psi, \sin\psi)$, *and* $\mathbf{r} - \mathbf{r}' = |\mathbf{r} - \mathbf{r}'|(\cos\phi', \sin\phi')$. *If* $\mathbf{a}_n$ *satisfies* $|k_{\text{b}}||\mathbf{a}_n - \mathbf{r}| \gg 0.25$

for $n = 1, 2, \cdots, N$ and $\mathbf{r} \in \Omega$, $\mathfrak{F}_{\mathrm{BFM}}(\mathbf{r}, C)$ can be represented as follows:

$$\mathfrak{F}_{\mathrm{BFM}}(\mathbf{r}, C) = \left| \frac{ik_0^2 N^2}{4\omega\mu_0} \int_D \left(\frac{\varepsilon(\mathbf{r}') - \varepsilon_{\mathrm{b}}}{\varepsilon_{\mathrm{b}}} + i\frac{\sigma(\mathbf{r}') - \sigma_{\mathrm{b}}}{\omega\varepsilon_{\mathrm{b}}} \right) \left(\mathcal{E}_1(k_{\mathrm{b}}, \mathbf{r}') - \frac{\mathcal{E}_2(k_{\mathrm{b}}, \mathbf{r}')}{N} \right) \mathrm{d}\mathbf{r}' \right. \tag{3.1}$$

$$\left. + CN \left(J_0(2k_{\mathrm{b}}|\mathbf{r}|) + \frac{1}{N} \sum_{n=1}^{N} \sum_{p=-\infty, p\neq 0}^{\infty} i^p J_p(2k_{\mathrm{b}}|\mathbf{r}|) \exp(ip\psi) \right) \right|, \tag{3.2}$$

where

$$\mathcal{E}_1(k_{\mathrm{b}}, \mathbf{r}') = \left(J_0(k_{\mathrm{b}}|\mathbf{r} - \mathbf{r}'|) + \frac{1}{N} \sum_{n=1}^{N} \sum_{p=-\infty, p\neq 0}^{\infty} i^p J_p(k_{\mathrm{b}}|\mathbf{r} - \mathbf{r}'|) \exp\left(ip(\theta_n - \phi') \right) \right)^2$$

and

$$\mathcal{E}_2(k_{\mathrm{b}}, \mathbf{r}') = J_0(2k_{\mathrm{b}}|\mathbf{r} - \mathbf{r}'|) + \frac{1}{N} \sum_{n=1}^{N} \sum_{p=-\infty, p\neq 0}^{\infty} i^p J_p(2k_{\mathrm{b}}|\mathbf{r} - \mathbf{r}'|) \exp\left(ip(\theta_n - \phi') \right).$$

Here, J_p denotes pth-order Bessel function of the first kind.

Proof. Following [26], $\mathrm{E}_{\mathrm{inc}}^{(z)}$ can be represented by the 2D Green's function:

$$\mathrm{E}_{\mathrm{inc}}^{(z)}(\mathbf{r}, \mathbf{r}') = -\frac{i}{4} H_0^{(1)}(k_{\mathrm{b}}|\mathbf{r} - \mathbf{r}'|), \quad \mathbf{r} \neq \mathbf{r}',$$

where $H_0^{(1)}$ denotes the zero-order Hankel function of the first kind. Since $|k_{\mathrm{b}}||\mathbf{a}_n - \mathbf{r}| \gg 0.25$ for all n, the following asymptotic form holds (see [27] for instance):

$$H_0^{(1)}(k_{\mathrm{b}}|\mathbf{a}_n - \mathbf{r}|) \approx \frac{(1-i)\exp(ik_{\mathrm{b}}|\mathbf{a}_n|)}{\sqrt{k_{\mathrm{b}}\pi|\mathbf{a}_n|}} \exp(-ik_{\mathrm{b}}\boldsymbol{\theta}_n \cdot \mathbf{r}). \tag{3.3}$$

Now, let us decompose the scattering matrix $\mathbb{K}(C)$ as

$$\mathbb{K}(C) = \mathbb{S} - \mathbb{D} + \mathbb{C},$$

where $\mathbb{S}$ is given by (2.4),

$$\mathbb{D} = \begin{bmatrix} S_{\mathrm{scat}}(1,1) & 0 & \cdots & 0 \\ 0 & S_{\mathrm{scat}}(2,2) & \cdots & 0 \\ \vdots & \vdots & \ddots & \vdots \\ 0 & 0 & \cdots & S_{\mathrm{scat}}(N,N) \end{bmatrix}, \quad \text{and} \quad \mathbb{C} = \begin{bmatrix} C & 0 & \cdots & 0 \\ 0 & C & \cdots & 0 \\ \vdots & \vdots & \ddots & \vdots \\ 0 & 0 & \cdots & C \end{bmatrix}.$$

First, by combining (2.3), (2.6), (2.7), and (3.3), we can find that

$$\begin{aligned}\mathbf{G}(\mathbf{r})\mathbb{S}\mathbf{G}(\mathbf{r})^T &= \sum_{n=1}^{N}\sum_{m=1}^{M}\frac{S_{\mathrm{scat}}(n,m)}{\mathrm{E}_{\mathrm{inc}}^{(z)}(\mathbf{a}_m,\mathbf{r})\mathrm{E}_{\mathrm{inc}}^{(z)}(\mathbf{r},\mathbf{a}_n)}\\ &= \frac{ik_0^2}{4\omega\mu_0}\sum_{n=1}^{N}\sum_{m=1}^{M}\int_D\left(\frac{\varepsilon(\mathbf{r}')-\varepsilon_{\mathrm{b}}}{\varepsilon_{\mathrm{b}}}+i\frac{\sigma(\mathbf{r}')-\sigma_{\mathrm{b}}}{\omega\varepsilon_{\mathrm{b}}}\right)\frac{\mathrm{E}_{\mathrm{inc}}^{(z)}(\mathbf{a}_m,\mathbf{r}')}{\mathrm{E}_{\mathrm{inc}}^{(z)}(\mathbf{a}_m,\mathbf{r})}\frac{\mathrm{E}_{\mathrm{inc}}^{(z)}(\mathbf{r}',\mathbf{a}_n)}{\mathrm{E}_{\mathrm{inc}}^{(z)}(\mathbf{r},\mathbf{a}_n)}\mathrm{d}\mathbf{r}'\\ &\approx \frac{ik_0^2}{4\omega\mu_0}\int_D\left(\frac{\varepsilon(\mathbf{r}')-\varepsilon_{\mathrm{b}}}{\varepsilon_{\mathrm{b}}}+i\frac{\sigma(\mathbf{r}')-\sigma_{\mathrm{b}}}{\omega\varepsilon_{\mathrm{b}}}\right)\left(\sum_{n=1}^{N}\exp\left(ik_{\mathrm{b}}\boldsymbol{\theta}_n\cdot(\mathbf{r}-\mathbf{r}')\right)\right)^2\mathrm{d}\mathbf{r}'.\end{aligned}$$

Since $\boldsymbol{\theta}_n\cdot k_{\mathrm{b}}(\mathbf{r}-\mathbf{r}') = k_{\mathrm{b}}|\mathbf{r}-\mathbf{r}'|\cos(\theta_n-\phi')$ and the following Jacobi–Anger expansion holds uniformly

$$\exp(ir\cos\theta) = J_0(r)+\sum_{p=-\infty,p\neq 0}^{\infty} i^p J_p(r)\exp(ip\theta),$$

we can obtain

$$\begin{aligned}&\sum_{n=1}^{N}\exp\left(ik_{\mathrm{b}}\boldsymbol{\theta}_n\cdot(\mathbf{r}-\mathbf{r}')\right) = \sum_{n=1}^{N}\exp\left(k_{\mathrm{b}}|\mathbf{r}-\mathbf{r}'|\cos(\theta_n-\phi')\right)\\ &\quad= N\left(J_0(k_{\mathrm{b}}|\mathbf{r}-\mathbf{r}'|)+\frac{1}{N}\sum_{n=1}^{N}\sum_{p=-\infty,p\neq 0}^{\infty} i^p J_p(k_{\mathrm{b}}|\mathbf{r}-\mathbf{r}'|)\exp\left(ip(\theta_n-\phi')\right)\right)\\ &\quad:= N\left(J_0(k_{\mathrm{b}}|\mathbf{r}-\mathbf{r}'|)+\frac{1}{N}\Phi(k_{\mathrm{b}},\mathbf{r}')\right).\end{aligned}$$

Correspondingly,

$$\begin{aligned}&\mathbf{G}(\mathbf{r})\mathbb{S}\mathbf{G}(\mathbf{r})^T\\ &\quad\approx \frac{ik_0^2N^2}{4\omega\mu_0}\int_D\left(\frac{\varepsilon(\mathbf{r}')-\varepsilon_{\mathrm{b}}}{\varepsilon_{\mathrm{b}}}+i\frac{\sigma(\mathbf{r}')-\sigma_{\mathrm{b}}}{\omega\varepsilon_{\mathrm{b}}}\right)\left(J_0(k_{\mathrm{b}}|\mathbf{r}-\mathbf{r}'|)+\frac{1}{N}\Phi(k_{\mathrm{b}},\mathbf{r}')\right)^2\mathrm{d}\mathbf{r}'.\end{aligned}\tag{3.4}$$

Next, similar to the derivation of (3.4), we can derive

$$\begin{aligned}&\mathbf{G}(\mathbf{r})\mathbb{D}\mathbf{G}(\mathbf{r})^T\\ &= \frac{ik_0^2}{4\omega\mu_0}\sum_{n=1}^{N}\int_D\left(\frac{\varepsilon(\mathbf{r}')-\varepsilon_{\mathrm{b}}}{\varepsilon_{\mathrm{b}}}+i\frac{\sigma(\mathbf{r}')-\sigma_{\mathrm{b}}}{\omega\varepsilon_{\mathrm{b}}}\right)\left(\frac{\mathrm{E}_{\mathrm{inc}}^{(z)}(\mathbf{r}',\mathbf{a}_n)}{\mathrm{E}_{\mathrm{inc}}^{(z)}(\mathbf{r},\mathbf{a}_n)}\right)^2\mathrm{d}\mathbf{r}'\\ &\approx \frac{ik_0^2}{4\omega\mu_0}\int_D\left(\frac{\varepsilon(\mathbf{r}')-\varepsilon_{\mathrm{b}}}{\varepsilon_{\mathrm{b}}}+i\frac{\sigma(\mathbf{r}')-\sigma_{\mathrm{b}}}{\omega\varepsilon_{\mathrm{b}}}\right)\sum_{n=1}^{N}\exp\left(2ik_{\mathrm{b}}\boldsymbol{\theta}_n\cdot(\mathbf{r}-\mathbf{r}')\right)\mathrm{d}\mathbf{r}'\\ &= \frac{ik_0^2N}{4\omega\mu_0}\int_D\left(\frac{\varepsilon(\mathbf{r}')-\varepsilon_{\mathrm{b}}}{\varepsilon_{\mathrm{b}}}+i\frac{\sigma(\mathbf{r}')-\sigma_{\mathrm{b}}}{\omega\varepsilon_{\mathrm{b}}}\right)\left(J_0(2k_{\mathrm{b}}|\mathbf{r}-\mathbf{r}'|)+\frac{1}{N}\Phi(2k_{\mathrm{b}},\mathbf{r}')\right)\mathrm{d}\mathbf{r}'.\end{aligned}\tag{3.5}$$

Finally, similar to the derivation of (3.5), we get

$$\begin{aligned}\mathbf{G}(\mathbf{r})\mathbb{C}\mathbf{G}(\mathbf{r})^T &= \sum_{n=1}^{N}\sum_{m=1}^{M}\frac{C}{\mathrm{E}_{\mathrm{inc}}^{(z)}(\mathbf{a}_m,\mathbf{r})\mathrm{E}_{\mathrm{inc}}^{(z)}(\mathbf{r},\mathbf{a}_n)}\\ &\approx C\sum_{n=1}^{N}\exp(2ik_{\mathrm{b}}\boldsymbol{\theta}_n\cdot\mathbf{r}) \qquad (3.6)\\ &= CN\bigg(J_0(2k_{\mathrm{b}}|\mathbf{r}|)+\frac{1}{N}\sum_{n=1}^{N}\sum_{p=-\infty,p\neq 0}^{\infty}i^pJ_p(2k_{\mathrm{b}}|\mathbf{r}|)\exp(ip\psi)\bigg).\end{aligned}$$

Therefore, by combining (3.4), (3.5), and (3.6), we obtain the result. □

Remark 3.1 (Selection of Constant Zero). Based on Theorem 3.1, we see that since $J_0(0)=1$ and $J_p(0)=0$ for nonzero p, the factor $\mathcal{E}_1(k_{\mathrm{b}},\mathbf{r}')-\mathcal{E}_2(k_{\mathrm{b}},\mathbf{r}')/N$ contributes to the detection of object but the factor of (3.2)

$$\Psi(k_{\mathrm{b}},\mathbf{r})=J_0(2k_{\mathrm{b}}|\mathbf{r}|)+\frac{1}{N}\sum_{n=1}^{N}\sum_{p=-\infty,p\neq 0}^{\infty}i^pJ_p(2k_{\mathrm{b}}|\mathbf{r}|)\exp(ip\psi)$$

does not contribute to object identification. Notice that if the following relation holds

$$C|\Psi(k_{\mathrm{b}},\mathbf{r})|\leq\frac{k_0^2(N-1)}{4\omega\mu_0}\bigg(\frac{\varepsilon_s-\varepsilon_{\mathrm{b}}}{\varepsilon_{\mathrm{b}}}+i\frac{\sigma_s-\sigma_{\mathrm{b}}}{\omega\varepsilon_{\mathrm{b}}}\bigg)\mathrm{area}(D_s), \qquad (3.7)$$

we can identify D_s through the map of $\mathfrak{F}_{\mathrm{BFM}}(\mathbf{r},C)$ because the disturbing term $CN\Psi(k_{\mathrm{b}},\mathbf{r})$ of (3.2) is dominated by the contributing terms of (3.1). This means that the imaging performance of $\mathfrak{F}_{\mathrm{BFM}}(\mathbf{r},C)$ depends significantly on the value of C. Unfortunately, we cannot select C to satisfy (3.7) without a priori information of the objects unless $C=0$. Therefore, the selection of $C=0$ guarantees object detection through the map of $\mathfrak{F}_{\mathrm{BFM}}(\mathbf{r},0)$. Since the value of $\mathfrak{F}_{\mathrm{BFM}}(\mathbf{r},0)$ reaches its maximum value when $\mathbf{r}=\mathbf{r}'\in D$, we can obtain the following result of unique determination.

Corollary 3.2 (Unique Determination of Objects)**.** *Under the same condition as that applied for Theorem 3.1, objects D_s can be determined uniquely through the map of $\mathfrak{F}_{\mathrm{BFM}}(\mathbf{r},0)$.*

4. Simulation Results With Synthetic and Real Data

To demonstrate the theoretical result in Section 3, some numerical simulation results with synthetic and real data at $f=925\,\mathrm{MHz}$ are provided here. The following normalized imaging function was applied throughout the following discussions:

$$\mathfrak{F}_{\mathrm{BFM}}(\mathbf{r},C)=\frac{|\mathbf{G}(\mathbf{r})\mathbb{K}(C)\mathbf{G}(\mathbf{r})^T|}{\max\limits_{\mathbf{r}\in\Omega}|\mathbf{G}(\mathbf{r})\mathbb{K}(C)\mathbf{G}(\mathbf{r})^T|}.$$

4.1. **Synthetic Data Experiment.** First, we considered the imaging result of $\mathfrak{F}_{\mathrm{BFM}}(\mathbf{r}, C)$ with synthetic data generated by CST STUDIO SUITE. To this end, we used $N = 16$ dipole antennas $\mathcal{A}_n$ equally distributed on a circle with a radius of $0.09\,\mathrm{m}$ to collect the measurement data. The region Ω was a circle of radius $0.085\,\mathrm{m}$ centered at the origin with material properties given by $(\varepsilon_{\mathrm{b}}, \sigma_{\mathrm{b}}) = (20\varepsilon_0, 0.2\,\mathrm{S/m})$, where $\varepsilon_0 = 8.854 \times 10^{-12}\,\mathrm{F/m}$ denotes vacuum permittivity.

Figure 1 shows the maps of $\mathfrak{F}_{\mathrm{BFM}}(\mathbf{r}, C)$ with various selections of C in the presence of two circles with radii $0.01\,\mathrm{m}$, locations $\mathbf{r}_1 = (0.01\,\mathrm{m}, 0.03\,\mathrm{m})$ and $\mathbf{r}_2 = (-0.04\,\mathrm{m}, -0.04\,\mathrm{m})$, and material properties $(\varepsilon_1, \sigma_1) = (55\varepsilon_0, 1.2\,\mathrm{S/m})$ and $(\varepsilon_2, \sigma_2) = (45\varepsilon_0, 1.0\,\mathrm{S/m})$. From the simulation results, we recognize the existence and outline shape of the objects when $|C| \leq 0.005$. When $C = 0.01i$, two large peaks appeared at the locations of the two objects, and another large peak appeared at the origin. Therefore, it is very difficult to distinguish the object. If $C = 0.01$, the two objects cannot be identified. Moreover, it is impossible to recognize the existence of objects when $C = 0.05i$. Hence, in this example, the existence and shape of objects can be retrieved through the map of $\mathfrak{F}_{\mathrm{BFM}}(\mathbf{r}, C)$ when $|C| \leq 0.005$.

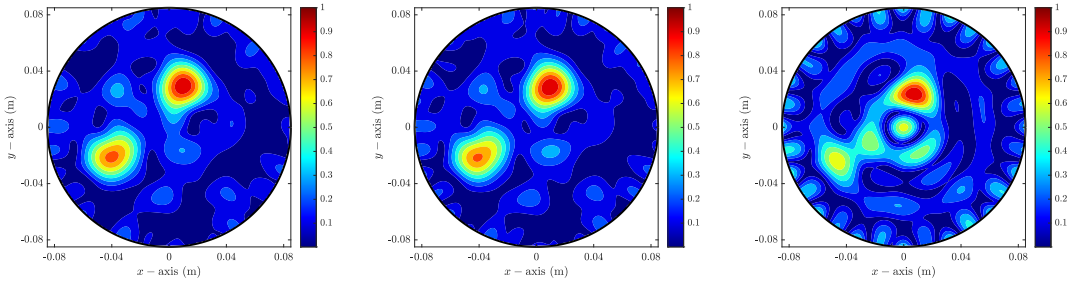

(a) $C = 0$ (b) $C = 0.001$ (c) $C = 0.01$

(d) $C = 0.005i$ (e) $C = 0.01i$ (f) $C = 0.05i$

FIGURE 1. Maps of $\mathfrak{F}_{\mathrm{BFM}}(\mathbf{r}, C)$ with various values of C.

4.2. **Real Data Experiment.** Next, we consider the imaging result of $\mathfrak{F}_{\mathrm{BFM}}(\mathbf{r}, C)$ with real data generated by a microwave machine. We refer to [18] for a detailed description of the

machine and simulation configuration. The region Ω was set to a circle of radius $0.085\,\mathrm{m}$ centered at the origin with material properties $(\varepsilon_\mathrm{b}, \sigma_\mathrm{b}) = (78\varepsilon_0, 0.2\,\mathrm{S/m})$.

Figure 2 shows maps of $\mathfrak{F}_{\mathrm{BFM}}(\mathbf{r}, C)$ with various values of C in the presence of the cross section of a screw driver of radius $0.003\,275\,\mathrm{m}$ located at $\mathbf{r} = (0.018\,\mathrm{m}, -0.018\,\mathrm{m})$. In contrast to the synthetic data experiment, the existence and outline shape of the object when $|C| \leq 0.00001$. Notice that when $C = 0.00005i$, two large peaks appeared at the location of the object and the origin, making it difficult to identify the object. If $|C| \geq 0.0001$, identification becomes impossible. Hence, in this example, we obtain reliable results when $|C| \leq 0.00001$.

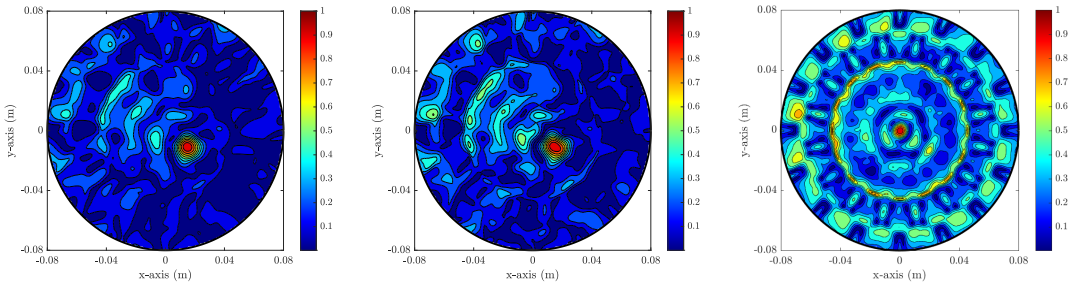

(a) $C = 0$ (b) $C = 0.00001$ (c) $C = 0.0001$

(d) $C = 0.000005i$ (e) $C = 0.00005i$ (f) $C = 0.0001i$

FIGURE 2. Maps of $\mathfrak{F}_{\mathrm{BFM}}(\mathbf{r}, C)$ with various values of C.

4.3. **Converting Zero Constant.** The synthetic and real data experiments showed that we obtain good results if the $|C|$ value is extremely small or close to zero. However, the criteria for *small enough* and *close to zero* is ambiguous, and the selection of constant C depends significantly on the simulation configuration (applied frequency of operation, material properties, etc.). Hence, we concluded that as discussed in Remark 3.1, converting unknown data as constant zero (i.e., $C = 0$) is the best choice for the proper application of the BFM in microwave imaging.

5. Conclusion

We considered the BFM for a fast identification of small objects from the measured scattered-field $S-$parameter data. The imaging function of the BFM was designed by converting the unknown diagonal elements of the scattering matrix into a fixed constant. From the formula of the scattered-field $S-$parameter data, we confirmed that the imaging function can be represented by an infinite series of Bessel functions of integer order, the antenna settings, the material properties, and the applied constant. Following the theoretical and numerical results, we concluded that the imaging performance depends significantly on the value of the constant, and the best choice for converting unknown data is the zero constant.

In this study, we explored 2D microwave imaging with full-aperture synthetic and real data. We believe that the analysis and numerical simulation can be extended to the limited-aperture measurement data [28]; we will explore this aspect in future work. Moreover, extending this approach to three-dimensional microwave imaging will be a valuable research subject.

Acknowledgments

This research was supported by the National Research Foundation of Korea (NRF) grant funded by the Korea government (MSIT) (NRF-2020R1A2C1A01005221, RS-2023-00242528), the research program of Kookmin University, and a New Faculty Research Grant of Pusan National University, 2024.

References

[1] R. Kress, *Inverse scattering from an open arc*, Mathematical Methods in the Applied Sciences, **18** (1995), 267–293.

[2] S. Ahmad, T. Strauss, S. Kupis, and T. Khan, *Comparison of statistical inversion with iteratively regularized Gauss Newton method for image reconstruction in electrical impedance tomography*, Applied Mathematics and Computation, **358** (2019), 436–448.

[3] R. Palmeri, M. T. Bevacqua, L. Crocco, T. Isernia, and L. D. Donato, *Microwave imaging via distorted iterated virtual experiments*, IEEE Transactions on Antennas and Propagation, **65** (2017), 829–838.

[4] F. Delbary, K. Erhard, R. Kress, R. Potthast, and J. Schulz, *Inverse electromagnetic scattering in a two-layered medium with an application to mine detection*, Inverse Problems, **24** (2008), Article No. 015002.

[5] O. Dorn and D. Lesselier, *Level set methods for inverse scattering*, Inverse Problems, **22** (2006), R67–R131.

[6] K. Ito, B. Jin, and J. Zou, *A direct sampling method to an inverse medium scattering problem*, Inverse Problems, **28** (2012), Article No. 025003.

[7] W.-K. Park, *A novel study on the orthogonality sampling method in microwave imaging without background information*, Applied Mathematics Letters, **145** (2023), Article No. 108766.

[8] S. Coşğun, E. Bilgin, and M. Çayören, *Microwave imaging of breast cancer with factorization method: SPIONs as contrast agent*, Medical Physics, **47** (2020), 3113–3122.

[9] S.-H. Son, K.-J. Lee, and W.-K. Park, *Real-time tracking of moving objects from scattering matrix in real-world microwave imaging*, AIMS Mathematics, **9** (2024), 13570–13588.

[10] W.-K. Park, *Real-time detection of small anomaly from limited-aperture measurements in real-world microwave imaging*, Mechanical Systems and Signal Processing, **171** (2022), Article No. 108937.

[11] W.-K. Park, *Application of MUSIC algorithm in real-world microwave imaging of unknown anomalies from scattering matrix*, Mechanical Systems and Signal Processing, **153** (2021), Article No. 107501.

[12] P. Monk, M. Pena, and V. Selgas, *Multifrequency linear sampling method on experimental datasets*, IEEE Transactions on Antennas and Propagation, **71** (2023), 8788–8798.
[13] W.-K. Park, *Investigation of a non-iterative technique based on topological derivatives for fast localization of small conductivity inclusions*, Computers & Mathematics with Applications, **120** (2022), 45–59.
[14] L. Jofre, A. P. Toda, J. M. J. Montana, P. C. Carrascosa, J. Romeu, S. Blanch, and A. Cardama, *UWB short-range bifocusing tomographic imaging*, IEEE Transactions on Instrumentation and Measurement, **57** (2008), 2414–2420.
[15] L. Jofre, A. Broquetas, J. Romeu, S. Blanch, A. P. Toda, X. Fabregas, and A. Cardama, *UWB tomographic radar imaging of penetrable and impenetrable objects*, Proceedings of the IEEE, **97** (2009), 451–464.
[16] Y. J. Kim, L. Jofre, F. D. Flaviis, and M. Q. Feng, *Microwave reflection tomographic array for damage detection of civil structures*, IEEE Transactions on Antennas and Propagation, **51** (2003), 3022–3032.
[17] S. Kang and W.-K. Park, *A novel study on the bifocusing method in two-dimensional inverse scattering problem*, AIMS Mathematics, **8** (2023), 27080–27112.
[18] J.-Y. Kim, K.-J. Lee, B.-R. Kim, S.-I. Jeon, and S.-H. Son, *Numerical and experimental assessments of focused microwave thermotherapy system at 925 MHz*, ETRI Journal, **41** (2019), 850–862.
[19] C. Y. Ahn, S. Chae, S. Kang, K.-J. Lee, W.-K. Park, and S.-H. Son, *Orthogonality sampling method for identifying small anomalies in real-world microwave imaging*, East Asian Journal on Applied Mathematics, **14** (2024), 293–313.
[20] S. Kang, W.-K. Park, and S.-H. Son, *A qualitative analysis of the bifocusing method for a real-time anomaly detection in microwave imaging*, Computers & Mathematics with Applications, **137** (2023), 93–101.
[21] W.-K. Park, *Real-time microwave imaging of unknown anomalies via scattering matrix*, Mechanical Systems and Signal Processing, **118** (2019), 658–674.
[22] W.-K. Park, *On the application of orthogonality sampling method for object detection in microwave imaging*, IEEE Transactions on Antennas and Propagation, **71** (2023), 934–946.
[23] S.-H. Son, K.-J. Lee, and W.-K. Park, *Application and analysis of direct sampling method in real-world microwave imaging*, Applied Mathematics Letters, **96** (2019), 47–53.
[24] S.-H. Son and W.-K. Park, *Application of the bifocusing method in microwave imaging without background information*, Journal of the Korean Society for Industrial and Applied Mathematics, **27** (2023), 109–122.
[25] M. Haynes, J. Stang, and M. Moghaddam, *Real-time microwave imaging of differential temperature for thermal therapy monitoring*, IEEE Transactions on Biomedical Engineering, **61** (2014), 1787–1797.
[26] W.-K. Park, H. P. Kim, K.-J. Lee, and S.-H. Son, *MUSIC algorithm for location searching of dielectric anomalies from $S-$parameters using microwave imaging*, Journal of Computational Physics, **348** (2017), 259–270.
[27] D. Colton and R. Kress, *Inverse Acoustic and Electromagnetic Scattering Problems*, Mathematics and Applications Series 93, Springer, New York, 1998.
[28] K. Belkebir and M. Saillard, *Special section: Testing inversion algorithms against experimental data*, Inverse Problems, **17** (2001), 1565–1571.